



Additive manufacturing of polymeric scaffolds for biomimetic cell membrane engineering

Sabaté Rovira, David; Nielsen, Hanne Mørck; Taboryski, Rafael; Bunea, Ada Ioana

Published in:
Materials and Design

Link to article, DOI:
[10.1016/j.matdes.2021.109486](https://doi.org/10.1016/j.matdes.2021.109486)

Publication date:
2021

Document Version
Publisher's PDF, also known as Version of record

[Link back to DTU Orbit](#)

Citation (APA):
Sabaté Rovira, D., Nielsen, H. M., Taboryski, R., & Bunea, A. I. (2021). Additive manufacturing of polymeric scaffolds for biomimetic cell membrane engineering. *Materials and Design*, 201, Article 109486. <https://doi.org/10.1016/j.matdes.2021.109486>

General rights

Copyright and moral rights for the publications made accessible in the public portal are retained by the authors and/or other copyright owners and it is a condition of accessing publications that users recognise and abide by the legal requirements associated with these rights.

- Users may download and print one copy of any publication from the public portal for the purpose of private study or research.
- You may not further distribute the material or use it for any profit-making activity or commercial gain
- You may freely distribute the URL identifying the publication in the public portal

If you believe that this document breaches copyright please contact us providing details, and we will remove access to the work immediately and investigate your claim.



Additive manufacturing of polymeric scaffolds for biomimetic cell membrane engineering

David Sabaté Rovira^a, Hanne Mørck Nielsen^b, Rafael Taboryski^a, Ada-Ioana Bunea^{a,*}

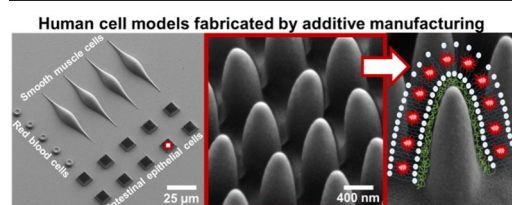
^a National Centre for Nano Fabrication and Characterization (DTU Nanolab), Technical University of Denmark, Ørsted Plads 347, 2800 Kgs. Lyngby, Denmark

^b Center for Biopharmaceuticals and Biobarriers in Drug Delivery, Department of Pharmacy, Faculty of Health and Medical Sciences, University of Copenhagen, Universitetsparken 2, 2100 Copenhagen Ø, Denmark

HIGHLIGHTS

- Biomimetic cell scaffolds were fabricated by additive manufacturing using direct laser writing two-photon polymerization
- Different design parameters were considered and tested to produce cell-like polyacrylate scaffolds with the wanted properties
- The polyacrylate scaffolds were modified with a lipid bilayer supported on a cationic polymer to mimic human cell membranes
- This interdisciplinary approach highlights the value of additive manufacturing for biomedical research

GRAPHICAL ABSTRACT



ARTICLE INFO

Article history:

Received 15 October 2020

Received in revised form 11 January 2021

Accepted 12 January 2021

Available online 15 January 2021

Keywords:

Additive manufacturing

Two-photon polymerization

3D design

Surface modification

Model cell membrane

ABSTRACT

Additive manufacturing based on direct laser writing two-photon polymerization facilitates the fabrication of microstructures with full 3D design freedom. Here, this fabrication technique is exploited for engineering scaffolds accurately mimicking the shape and size of three types of human cells. The human cell models employed in the study were chosen to include a range of dimensions and different identifiable features to highlight the versatility of this fabrication approach, yet other cell shapes can easily be fabricated in similar manner. The design and fabrication parameters for the additive manufacturing process were optimized to obtain polymeric scaffolds with biomimetic shapes. After fabrication, the cell scaffolds were converted to polymer-cushioned model cell membranes through layer-by-layer functionalization with a cationic polymer and a lipid bilayer. Scaffold functionalization was verified using confocal laser scanning microscopy. Polymer-cushioned model cell membranes supported on 3D scaffolds mimicking the shape of human cells are particularly suitable for membrane interaction studies where membrane curvature plays an important role. The aim of this study is to demonstrate the engineering of biomimetic cell membranes by high-resolution additive manufacturing combined with surface functionalization. The interdisciplinary approach highlights the value of additive manufacturing as technological solution for challenges encountered in biomedical studies.

© 2021 The Author(s). Published by Elsevier Ltd. This is an open access article under the CC BY license (<http://creativecommons.org/licenses/by/4.0/>).

Abbreviations: 2PP, two-photon polymerization; AM, additive manufacturing; CEC, columnar epithelial cell; CLSM, confocal laser scanning microscopy; Dil, 1,1'-dioctadecyl-3,3',3'-tetramethylindocarbocyanine perchlorate; DLW, direct laser writing; DOPC, 1,2-dioleoyl-sn-glycero-3-phosphocholine; GI, gastrointestinal; HEPES, 4-(2-hydroxyethyl)piperazine-1-ethanesulfonic acid; PETA, pentaerythritol triacrylate; PGMEA, propylene glycol monomethyl ether acetate; PLL, poly-L-lysine; RBC, red blood cell; SEM, scanning electron microscopy; SMC, smooth muscle cell; SUV, small unilamellar vesicle.

* Corresponding author at: Akademivej, Building 358, room 006, DK-2800 Kgs. Lyngby, Denmark.

E-mail address: adabu@dtu.dk (A.-I. Bunea).

1. Introduction

Originally introduced in the late 1980's as *rapid prototyping*, additive manufacturing (AM) [1] has become dramatically more popular and versatile in the past two decades. Whereas in its early years AM was useful mostly for making prototypes which facilitated parameter optimization, nowadays it is widely employed for manufacturing various components and final parts in a number of industry branches, including e.g. the biomedical, car manufacturing, aerospace engineering, or construction industries. Overall, different *flavours* of AM, such as fused filament fabrication, stereolithography, ink-jetting, selective laser sintering, or two-photon polymerization, enable the fabrication of objects with sizes spanning several orders of magnitude in materials ranging from soft polymers to ceramics and metals.

AM is increasingly used for fabricating scaffolds with applications in cell culture and tissue engineering [2–7] as part of a recently emerging field that is tentatively called *printing biology* [8]. A number of biocompatible materials [9,10] and biomaterials [11,12] suitable for AM processing are already available, while others are currently being developed by researchers around the world. Surface functionalization can also improve the suitability of structures fabricated by AM for various biomedical applications [13–16]. In addition to the use of the more widespread AM techniques that generate macroscopic structures, such as stereolithography [17] or fused filament fabrication [18], higher resolution AM techniques such as projection microstereolithography [19] or two-photon polymerization (2PP) direct laser writing (DLW) [20] are gaining momentum for the fabrication of microscale devices and scaffolds for biomedical applications [21–27]. Although it is more limited in terms of scale, 2PP features significantly higher resolution than all other AM techniques, enabling the DLW of objects with critical dimensions as small as 100–200 nm. Whereas early 2PP AM relied on relatively simple resins that could undergo two-photon absorption, there is a growing interest in the use of smart, stimuli-responsive materials [28–31], and in the DLW of multi-material structures [32].

Given the selection of available AM technologies and the huge range of materials that can thus be processed, there is a tremendous freedom of design in terms of object shape, size, chemical and mechanical properties [33]. Taking inspiration from nature can sometimes provide the quickest path to overcoming certain challenges, which is why one rather recent and important approach in AM is biomimicry. Biomimetic elements can come into play when it comes solely to the material design [34], or can apply to different properties of the object, including the object shape and topology [35–37].

When it comes to biomedical applications, the biocompatibility of structures fabricated by AM is often a critical element. Recent review papers discuss various material functions encountered in 2PP, including biocompatibility [20,38]. Typically, the toxicity of a resin comes from the photoinitiator component. Consequently, biocompatibility can sometimes be achieved simply by increasing the degree of conversion, which can be done by tailoring the fabrication process or by employing post-processing steps [20]. Furthermore, a number of biocompatible 2PP photoinitiators and resins have already been reported [20], and several biocompatible resin formulations for 2PP, such as IP-Visio or Ormosil, are commercially available. The main photoresist employed in this work, IP-L 780, was shown to have good biocompatibility in several studies, which employed it to fabricate scaffolds used for cell culture after surface functionalization [24,39].

One of the most investigated research fields from recent years is drug delivery, which is driven by its societal value. Oral administration of drugs ensures the highest patient compliance and convenience, but numerous challenges are nevertheless associated with oral drug delivery, which is why there is a huge interest in novel drug molecules and drug delivery systems for oral administration [40]. Any formulation administered orally moves through the gastrointestinal (GI) tract, where the active pharmaceutical ingredient is absorbed from the small intestine, and then further transported via the systemic circulation to its

target site. Most often, active pharmaceutical ingredients act by binding to receptors located either on the cell membrane, or inside the cell. Altogether, this means that drug molecules interact with various biological membranes one way or another before having the desired effect in the human body [41]. Thus, interactions with cell membranes found throughout the body play an important role in drug delivery [42]. Native cell membranes are rather hard to isolate and handle with a reproducible and reliable outcome, so model cell membranes have instead become the preferred method for studying the interactions between drugs and biological membranes. A tremendous number of model cell membranes of various complexity have been developed throughout the years [43,44], most of which are based on lipid bilayers [42]. Different membrane interaction studies require certain characteristics of the model cell membrane, as recently reviewed elsewhere [42]. Since cell membranes are highly complex and exhibit different composition and properties between different types of cells, there is no such thing as a perfect model cell membrane. Model cell membranes are simplified versions of their real life counterparts, so there can sometimes be a mismatch between expected results based on in vitro studies and the actual in vivo situation [45]. One of the cellular properties that is most often overlooked in designing model cell membranes is the cell shape, as this is rather complicated to account for. However, membrane curvature was reported to have an important effect on membrane properties, particularly in studies involving the conformation of transmembrane proteins [46–48]. A recent paper from Larsen et al. discussed the physical and molecular mechanisms underlying the correlation between geometry and function in biological membranes. Their detailed study showed that, in addition to the mean membrane curvature, the often-neglected Gaussian curvature is also an important factor for protein sorting in the membrane. This means that for the same mean curvature, membranes with e.g. spherical and cylindrical shapes will exhibit different behaviours [49]. Currently, studies that require curved model cell membranes typically employ vesicles [50], either in suspension, or immobilized on a solid substrate. However, under such circumstances vesicles are often quite physically unstable, and their immobilization on a solid substrate is particularly challenging [51]. Furthermore, vesicles are spherical and they consequently have a very different Gaussian curvature compared to human cells. Most importantly, there are no model cell membranes accurately reproducing human cell curvature reported to date. On the other hand, existing studies have already highlighted the importance of membrane curvature, so the development of model cell membranes with biomimetic shapes and dimensions is meant to be a novel technological solution to an existing challenge.

This paper presents a novel approach for engineering biomimetic cell membranes, in the form of polymer-cushioned lipid bilayers supported on polymeric scaffolds fabricated by 2PP AM. Such model cell membranes accurately mimic membrane curvature because the support scaffolds reproduce the shapes and sizes of actual cells. Therefore, these models should be particularly interesting for drug delivery studies where membrane curvature could be a critical factor. The design, fabrication, and characterization of three types of scaffolds with different biomimetic shapes and sizes are presented herein as examples, whereas the concept and techniques can easily be adapted to cover any other human cell models. In addition to the intestinal epithelial cell model, which is most relevant for oral drug delivery, we also present models for red blood cells and smooth muscle cells in order to demonstrate the versatility of the approach.

2. Materials and methods

2.1. Materials

The IP-L 780 and IP-Dip photoresists, 170 μm thick 30 mm \varnothing borosilicate glass coverslips, 0.7 mm thick 30 \times 30 mm² fused silica, and Immersol 518F immersion oil employed in the fabrication process were purchased from Nanoscribe (Karlsruhe, Germany). Isopropanol (99%),

ethanol (99.9%), and chloroform (99.9%) were purchased from VWR (Radnor, PA, USA). 1,2-Dioleoyl-*sn*-glycero-3-phosphocholine (DOPC) 18:1 solution in chloroform, propylene glycol monomethyl ether acetate (PGMEA), 4-(2-hydroxyethyl)piperazine-1-ethanesulfonic acid (HEPES, 1 M, 99.5%), poly-L-lysine (PLL, 0.1% w/v in H₂O) and 1,1'-dioctadecyl-3,3,3',3'-tetramethylindocarbocyanine perchlorate (DiI, 98%) were purchased from Merck, Darmstadt, Germany.

2.2. Design and fabrication of cell scaffolds

The 3D design of cell scaffolds was done in SolidWorks 2019 (Dassault Systèmes, Vélizy-Villacoublay, France) and the technical drawings are shown in Section S1 of the Supporting information (SI). The output .STL file was imported into the DeScribe software, version 2.5.5 (Nanoscribe, Karlsruhe, Germany), where the print parameters were set as described in Section S2 of the SI, and the .GWL job file for AM was generated. Arrays of the model cell structures were generated in DeScribe. Fabrication was done by direct laser writing (DLW) using two-photon polymerization (2PP) on a Nanoscribe GT+ system (Nanoscribe, Karlsruhe, Germany), which uses 150 fs pulses emitted at 100 MHz by a 780 nm Ti-Sapphire laser and focused into the sample through a Plan-APOCHROMAT 63×/1.40 Oil DIC objective (Carl Zeiss, Oberkochen, Germany). For all structures except the one shown in Fig. 5c, 170 μm thick borosilicate glass coverslips were used as AM substrates in *oil immersion* configuration, and the negative-tone commercial acrylic photoresist IP-L 780 was employed as polymer precursor. Prior to printing, the glass coverslips were cleaned by rinsing with ethanol and deionized water, and subsequently blow-dried with air. After printing, uncrosslinked IP-L 780 was removed by 20 min incubation in isopropanol. For the structure shown in Fig. 5c, 0.7 mm thick 30 × 30 mm² fused silica was used as printing substrate in *DiI* configuration, and the negative-tone commercial acrylic photoresist IP-Dip was employed as polymer precursor. After printing, uncrosslinked IP-Dip was removed by 20 min incubation in PGMEA, followed by 5 min incubation in isopropanol. For all samples, the substrate containing the fabricated structures was rinsed after development with deionized water and blow-dried with air. The fabrication process, including development and washing steps, was conducted at room temperature.

2.3. Preparation of small unilamellar vesicles

The small unilamellar vesicles (SUV) were prepared using the Bangham method [52] followed by extrusion using a protocol originally described by Mui et al. [53] Briefly, a solution of DOPC in chloroform was diluted in chloroform at a concentration of 10 mg·mL⁻¹. The fluorescent dye DiI was added to this mixture at a concentration of 0.3 mg·mL⁻¹. The organic solvent was then evaporated at room temperature under vacuum at a rotor evaporator, and the resulting lipid films were washed three times with ethanol, followed by overnight solvent evaporation after the last wash. The lipid films were rehydrated using HEPES buffer (10 mM, pH 7.4) at 40 °C for 1 h, with vortexing for 1 min every 10 min, and annealed at room temperature for 1 h, resulting in a lipid concentration of 2.5 mg·mL⁻¹. SUV were then obtained by 10 times extrusion at 40 °C through two polycarbonate filters with pore sizes of 100 nm (Whatman, Maidstone, UK) using a LIPEX extruder (TRANSFERRA Nanosciences, Vancouver, Canada).

2.4. Scaffold characterization using scanning electron microscopy

Scanning electron microscopy (SEM) was performed using a Zeiss Supra 40 VP (Carl Zeiss, Oberkochen, Germany) scanning electron microscope on fabricated samples coated with a thin gold layer (15–30 nm) using a sputter coater (Cressington Scientific Instruments, Watford, UK). All images were acquired using the secondary electron detector, a low acceleration voltage (1.0–1.5 kV) and high vacuum mode.

2.5. Scaffold characterization using profilometry

A 3D optical profiler confocal interference microscope (Sensofar Tech, Terrassa, Spain) equipped with a 50×/0.80 objective was used to characterize the height profile of the 3D printed samples. Using the 50×/0.80 objective, the field of view is 254.6 μm × 190.9 μm, and the pixel resolution limit is 1.51 μm [54].

2.6. Surface modification of the polymeric cell scaffolds

Surface modification was performed using a two-step protocol adapted from Wan et al. [55] In the first step, the 3D printed structures were incubated with a 1 mg·mL⁻¹ PLL solution for 20 min at room temperature. Unbound PLL was removed by washing twice with deionized water. In the second step, a 1 mg·mL⁻¹ DOPC SUV suspension was added to the PLL-modified polymeric structures and incubated for 20 min at room temperature. Excess SUV were removed by washing twice with deionized water, after which the sample was kept in HEPES buffer (10 mM, pH 7.4) overnight at 4 °C before subsequent characterization using confocal laser scanning microscopy (CLSM). Reference samples for CLSM constituted samples where the PLL incubation step was replaced by incubation with HEPES buffer (10 mM, pH 7.4), and otherwise prepared as described above.

2.7. Scaffold characterization using confocal laser scanning microscopy

CLSM was performed using a Zeiss Axio LSM 700 upright microscope (Carl Zeiss, Oberkochen, Germany) equipped with an EC Epiplan-Neofluar 20×/0.50 HD M27 objective (Carl Zeiss) and an AxioCam MRC camera (Carl Zeiss). All samples consisted of polymeric scaffolds supported on borosilicate glass coverslips and covered by a thin layer of HEPES buffer. In accordance with the producer specifications for the fluorescent dye DiI, the excitation wavelength was set to 549 nm and the emission wavelength to 565 nm using the electronic filters configured in the ZEN Black software (Carl Zeiss). CLSM images set to have 16 bit depth and a frame size of 1024 × 1024 pixels were acquired using a pixel dwell time of 3.15 μs and 4 frame averaging. All other acquisition parameters (pinhole size, laser power, gains) were initially optimized on a target sample, and the same settings were subsequently used for imaging all samples and corresponding references.

Data analysis of images acquired using CLSM was done in the ImageJ software [56] version 1.51j8 (public domain, developed at the National Institutes of Health, Madison, WI, USA). The fluorescence intensity profile was determined by drawing a straight line in ImageJ, followed by using the Plot Profile analysis function. The average fluorescence intensity for individual cell scaffolds was determined by first selecting the target scaffold unit using the Oval (RBC), Rectangular (CEC) or Free hand (SMC) Selection tools, followed by computing the mean gray value from the ImageJ Analyze tab. For every image, the mean gray value for 3 different cells was computed, together with the mean gray value of the background, and 3 separate images were used for each measurement. The average mean gray value for each type of sample was calculated by averaging individual measurements after subtracting the corresponding background mean gray value. All calculations and corresponding graphs were done in Origin 2018 version 95E (Origin Lab, Northampton, MA, USA). For the fluorescence images shown in Fig. 4, the background fluorescence was removed by using the Subtract Background function in ImageJ, a rolling ball radius of 100 pixels, and no smoothing.

3. Results and discussion

3.1. Design and fabrication of biomimetic cell scaffolds

The profiles of three types of human cells with different dimensions and features were chosen to demonstrate the versatility of the approach

presented herein for fabricating model cell membranes with realistic shapes and dimensions. The first type represents red blood cells (RBC), also known as erythrocytes. RBC are shaped as biconcave disks, i.e. disks with a thicker contour and a depression in the center. The average diameter of human RBC is $7.2\ \mu\text{m}$, with individual RBC typically ranging from 6.8 to $7.5\ \mu\text{m}$ [57], a size which places them among the smallest human cells. The second type of cells chosen is smooth muscle cells (SMC), also known as fibers. SMC are spindle-shaped, i.e. they are wider in the middle and tapered at both ends. In the relaxed state, they typically have a width of several micrometers and a length in the range of tens to hundreds of micrometers [58], which means they are rather large compared to most other human cells. Both RBC and SMC have relatively smooth surfaces, easily recognizable shapes and very different sizes, but no characteristic small topological features. The third type of cells chosen is columnar epithelial cells (CEC), also known as absorptive enterocytes, found in the GI tract in the small intestine. CEC consist of a rather large columnar body with a height in the order or tens of micrometers and a smaller lateral size of around $12\ \mu\text{m}$, and display a dense array of microvilli, on the apical surface of the epithelium facing the intestinal lumen. These microvilli are typically $100\ \text{nm}$ in diameter, $1\ \mu\text{m}$ high, and densely packed in a hexagonal array, with a spacing of around $100\ \text{nm}$ [59].

Fig. 1a, e, and i show rendered images of the designed RBC, SMC and CEC scaffold units, respectively. The design parameters were based on the average shape and size of the corresponding type of human cells and are shown in Section S1 of the SI. However, deviations from human cell parameters were made in order to improve the fabrication time and the adhesion to the substrate for the cell scaffolds designs. More specifically, in the case of RBC, the bottom side of the cell is designed to be flat instead of concave. For the SMC, the spindle-shaped structure is sliced equatorially, so that only half a cell with a flat base

is printed. In both cases, the flat base ensures strong adhesion to the substrate, which is a requirement for subsequent experiments, particularly for the surface modification steps. In the case of CEC, only the apical side of the cell, containing the microvilli, is printed, while the large columnar body is neglected. This reduces the print time tremendously, yet still enables access to the interesting topological features of these cells, i.e. the microvilli. Furthermore, the microvilli are designed to be larger and packed less densely than the ones found in nature. This is because the natural microvilli dimensions are beyond the resolution limit of AM. According to the producer's specifications, the highest resolution mode on the NanoScribe enables DLW of features of $\sim 200\ \text{nm}$ and requires a spacing of $>500\ \text{nm}$ to ensure feature separation. Nevertheless, all cell scaffold models can be considered to approximate reasonably the corresponding human cells.

Converting the 3D designs to fabrication files requires slicing and hatching of the structures in the DeScribe software. Previews of the printable 3D structures obtained in this manner are shown in Fig. 1b, f and j. Despite the high resolution of 2PP, the apparent smoothness of the designed structures is somewhat reduced when converting the .STL file to the printable .GWL file. To minimize this, contour lines were also included during the DeScribe file conversion (additional details in Section S2 of the SI).

When using the $63\times/1.40$ objective, the largest surface area that can be printed without displacing the stage and instead making use of the galvo mirrors is specified by the producer to be a circle with a diameter of $200\ \mu\text{m}$, which can inscribe a square of $140\times 140\ \mu\text{m}^2$. To avoid potential distortions near the edges, all chosen designs are printed in arrays of $120\times 120\ \mu\text{m}^2$, which fit well within the galvo range of the NanoScribe. Since RBC in the human body are found as free-floating cells in the blood, the RBC arrays are printed with relatively large spacing between individual cells. On the other hand, SMC and CEC are

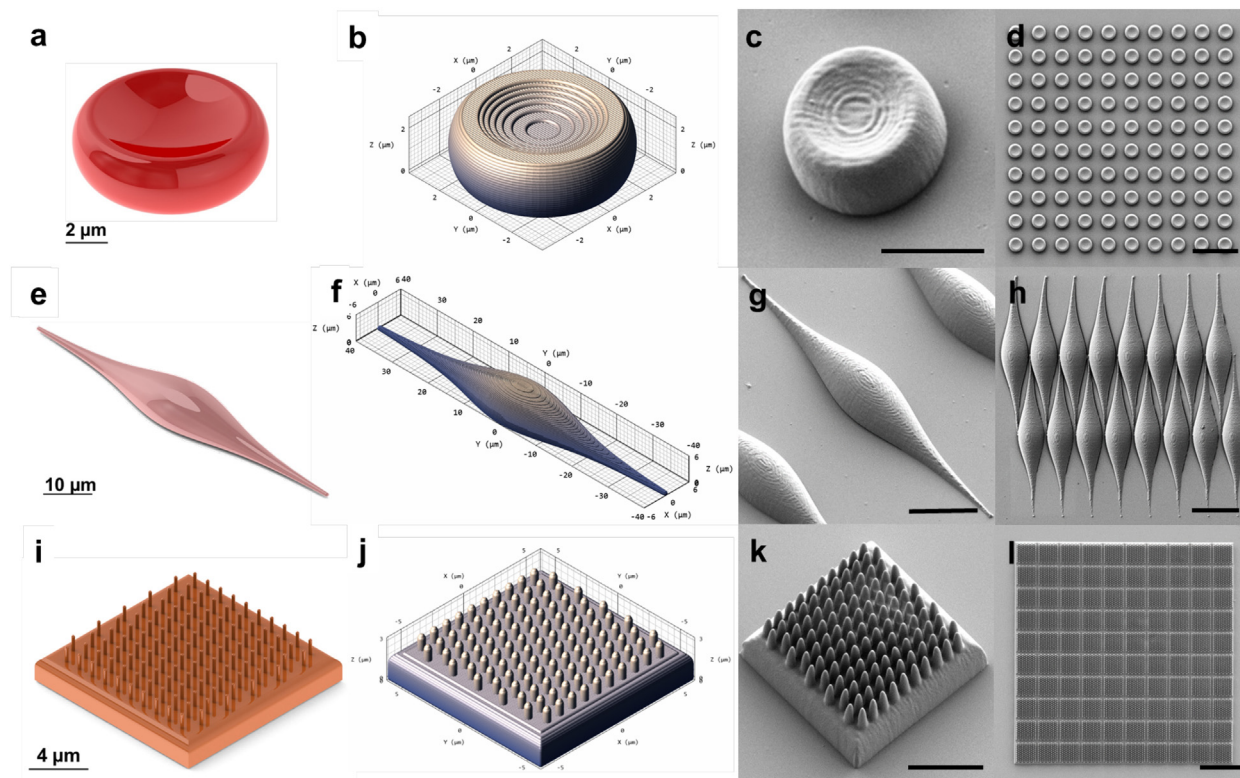


Fig. 1. Images showing the designed and fabricated cell scaffolds using additive manufacturing with optimized parameters. (a–d) Red blood cell (RBC) model. (e–h) Smooth muscle cell (SMC) model. (i–l) Ciliated columnar epithelial cell (CEC) model. (a, e, i) Rendered images of the 3D designs for a single cell. (b, f, j) Preview of a single cell generated in the DeScribe software after defining the parameters for the additive manufacturing fabrication process. Scanning electron micrographs of the fabricated (c, g, k) individual cells, acquired using a 30° stage tilt, scale bar is $5\ \mu\text{m}$, and (d, h, l) $120\times 120\ \mu\text{m}^2$ cell arrays, scale bar is $25\ \mu\text{m}$.

commonly found tightly packed in tissues, so the arrays were designed to reflect this. This can be observed in the micrographs in Fig. 1d, h and i, whereas the array designs are shown in Section S3 in the SI. The $120 \times 120 \mu\text{m}^2$ cell scaffold arrays were printed in ~ 6 min (RBC), ~ 2 min (SMC), and ~ 15 min (CEC). This confirms the suitability of using 2PP AM as fabrication technique for polymeric cell scaffolds of various shapes and sizes in a reasonable time frame. Further improving the 2PP AM fabrication speed can be achieved by replacing the 2PP point-by-point exposure with layer-by-layer exposure, as recently demonstrated by Saha et al. [60]

The fabricated 3D cell scaffolds match very well the expected outcome based on the job file, as confirmed by the micrographs shown in Fig. 1 and the measurements shown in Table S2 from Section S4 of the SI. The only noteworthy difference is the increased diameter of the microvilli features, from 200 nm in the 3D design to 550 ± 60 nm in the fabricated structures. However, this is an expected consequence of including contour lines during the 3D structure conversion to fabrication files. The voxel size for the laser writing process is ~ 200 nm. Adding a contour line to an object with a diameter of 200 nm requires the DLW of additional points surrounding the object. This naturally results in a total diameter of ~ 600 nm, since the contour line will add 200 nm on all sides of the object. This is not valid for larger structures, where the contour line instead simply follows the outermost layer of points generated during the hatching step.

It is already well established that the material properties, shape and topology of 2PP-fabricated structures can be tailored by choosing a specific photoresist, altering the parameters of the printing process, and by post-processing of the printed structures. While 2PP-processed polyacrylate structures have a Young modulus in the range of 5–5000 MPa following a quadratic relationship with density [61], a higher degree of conversion has been shown to lead to increased stiffness [62]. The degree of conversion is influenced by the laser power and writing speed used during the printing process, and thus adjusting the AM fabrication parameters offers a degree of freedom for tailoring the resulting structure stiffness. Furthermore, post-print curing has been shown to improve the mechanical properties by increasing the degree of crosslinking in polyacrylate-based structures [61] or polymers containing anthracene dimers [63].

Jiang et al. investigated the dependence of the IP-L 780 degree of conversion on laser power and writing speed using a Nanoscribe GT system [62]. A degree of conversion of 35% was determined from Raman microspectroscopy studies for a laser power of 12 mW and a writing speed of $40 \mu\text{m} \cdot \text{s}^{-1}$. From the Nanoscribe calibration file, we found that these parameters produce structures extremely similar to those produced with the settings used in this paper for printing using the newer Nanoscribe GT+ system, i.e. Galvo mode, 40% of the maximum laser power (~ 20 mW), and a writing speed of $10,000 \mu\text{m} \cdot \text{s}^{-1}$. Therefore, the 3D cell scaffolds presented herein are expected to have a degree of conversion of $\sim 35\%$. By changing the 2PP fabrication parameters, the degree of conversion of the polymer precursor solution can be expected to vary between 20% and 45% [64].

The polymer precursor in the Nanoscribe proprietary resins IP-L 780 and IP-Dip is pentaerythritol triacrylate (PETA) [61,65]. Recently, Bauer and co-workers performed a detailed study of the mechanical properties of PETA microstructures fabricated by two-photon polymerization using a Nanoscribe GT system [64]. Based on their experiments, for a degree of conversion of 35%, as is the case of our structures, it is expected that the yield strength σ is ~ 59 MPa, and the Young's modulus E is ~ 2.8 GPa [64].

Whereas the 3D printed microstructures presented in this work have a stiffness of a few GPa, cells are considerably softer. In human cells, the nanometer-thin lipid bilayer-based cell membrane surrounds the cytoplasm, which typically has a stiffness of only several kPa [66]. However, solid supports with high stiffness are often employed for building model cell membranes [42]. For example, the common glass coverslips have a stiffness of ~ 50 GPa [66]. Among other benefits, one

of the roles of the polymer cushion in the model cell membrane employed herein is to reduce the influence of the stiff substrate on the lipid bilayer membrane. Nevertheless, microstructured substrates of reduced stiffness should be explored in the future, as 2PP DLW of various soft materials and hydrogels has already been demonstrated [67–69]. Thus, we envision that 2PP AM could be employed to fabricate scaffolds that mimic not only the shape of human cells, but also their stiffness.

On the other hand, when rapid fabrication of large structures or arrays is needed, the print parameters, i.e. slicing and hatching distances, can be adjusted in order to increase the print speed. This leads to an increase in surface roughness, which can be compensated for by post-processing using thermal reflow [70]. Finally, for high-resolution structures, an option for decreasing the minimal feature size below 100 nm is post-processing using isotropic plasma etching and/or pyrolysis [71]. Overall, this shows that 2PP AM is flexible not only in terms of structure design, but also in terms of material properties, which can be tailored before the AM process through the choice of photoresist, during the AM process by altering the print parameters, and after the AM process through post-processing methods. This flexibility should ultimately enable the fabrication of truly biomimetic cell scaffolds that accurately reproduce not only the shape, but also the mechanical properties of their biological counterparts.

3.2. Optimization of the design and fabrication parameters

Before the biomimetic scaffolds shown in Fig. 1 could be manufactured with the desired quality, it was necessary to optimize a number of design and fabrication parameters. First, a parameter sweep was performed on the NanoScribe to identify the laser power and scan speed providing the best trade-off between resolution and fabrication speed. This was based on a standard test file provided by NanoScribe and is a typical step for all NanoScribe 2PP equipment, so it will not be further detailed herein. The voxel aspect ratio was set in the NanoScribe system according to the desired structure shape. In principle, the voxel dimensions and elongation could also be further optimized [72]. During the AM process of the 3D cell scaffolds, a number of challenges were identified. A selection of images from the optimization process of the design parameters for the different 3D scaffolds is shown in Fig. 2, and the different challenges and optimization steps undertaken are described below.

For RBC scaffolds, a discrepancy between the height of the designed and manufactured scaffolds was identified for the first design (Fig. 2a–c). Whereas the 3D design dictated a structure height of $2.5 \mu\text{m}$, optical profilometry showed the average height of the fabricated structures to be $5.7 \pm 0.4 \mu\text{m}$ (average \pm SD from 8 measurements). This could be attributed to the combination of setting a target voxel aspect ratio of 1.5 in the DeScribe software and using a base count number of 6 in the AM process. Thus, in order to manufacture RBC scaffolds with the biomimetic dimensions and reasonable smoothness, the base count was reduced to 0 and the voxel aspect ratio was kept at 1.5. In this manner, the RBC scaffolds with a height of $3.2 \pm 0.2 \mu\text{m}$ shown in Fig. 1d were produced. Although the target voxel aspect ratio was set in the system to 1.5, in practice this value is slightly higher, which in turn leads to a slightly higher structure height compared to the design. Using the predefined voxel aspect ratio of 3.5, would likely lead to structures with a height matching the design perfectly, but is expected to reduce the quality of the fine features, which is why it was not attempted.

In the case of SMC scaffolds, no unexpected challenges were identified. Nevertheless, the number of contour lines was optimized in order to obtain the desired structure smoothness (Fig. 2d–f). For SMC units with no contour lines, the hatching lines are quite prominent (Fig. 2d). Including one contour line helped overcome this, but it emphasized the layer slicing (Fig. 2e). Increasing the contour line count to five generated the smoothest SMC units (Fig. 2f), whereas further increasing the number of contour lines had no noticeable effect.

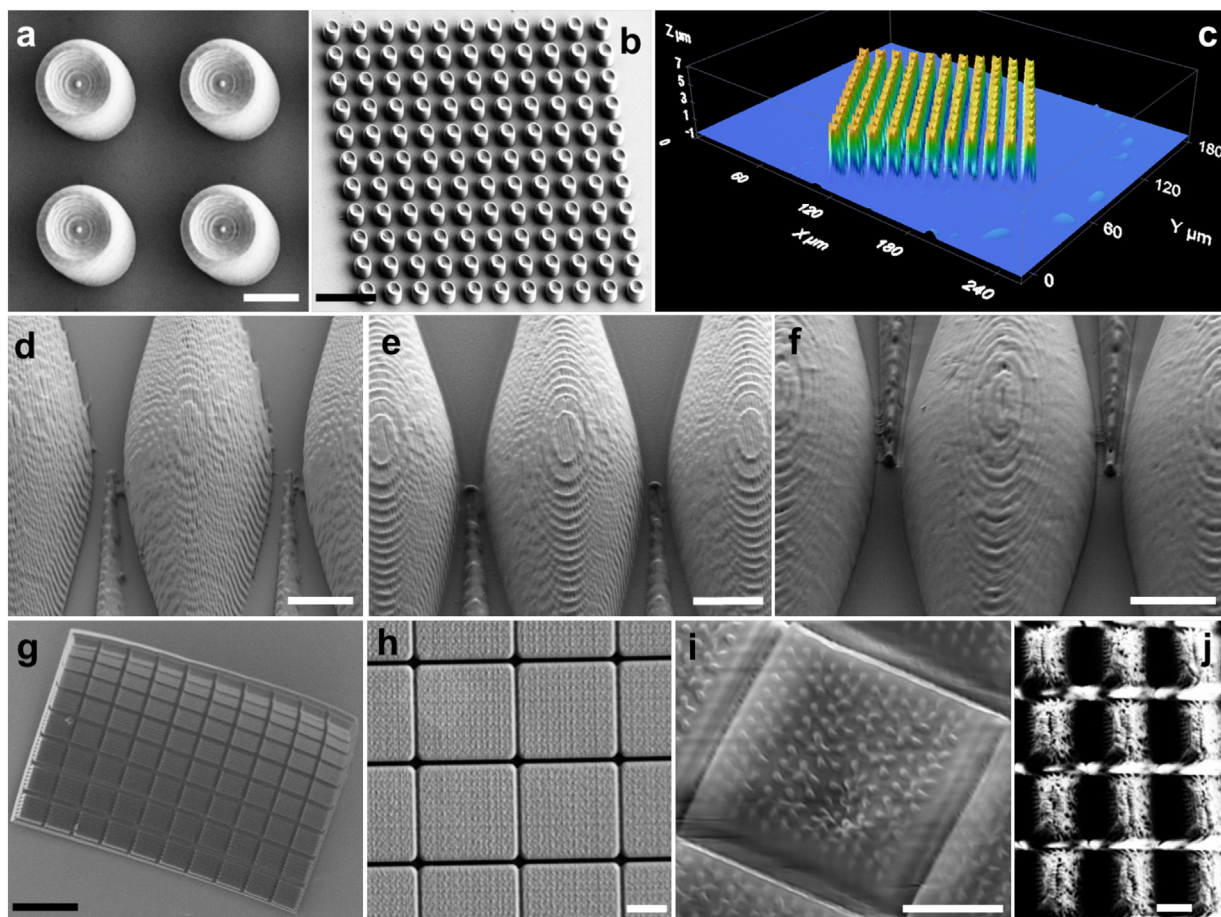


Fig. 2. Design optimization for (a-c) red blood cell (RBC) scaffolds, (d-f) smooth muscle cell (SMC) scaffolds, and (g-j) columnar epithelial cell (CEC) scaffolds. Defective RBC scaffolds with exaggerated height, as seen from (a, b) scanning electron micrographs and (c) a natural proportion image generated using optical profilometry. Scanning electron micrographs of SMC scaffolds fabricated using (d) 0, (e) 1 and (f) 5 contour lines. (g) Folded $120 \times 120 \mu\text{m}^2$ CEC array. (h, j) CEC scaffolds displaying poorly defined microvilli. Scale bar is (a, d, e, f, h, i, j) $5 \mu\text{m}$ and (b, g) $25 \mu\text{m}$.

As expected, AM of the CEC scaffolds was more challenging. An issue encountered with the first design was a folding of the $120 \times 120 \mu\text{m}^2$ CEC array (Fig. 2g). This was likely caused by stress in the thin polymer layer attached to the substrate. To overcome this challenge, increasing the thickness of the polymer base from $1 \mu\text{m}$ to $1.5 \mu\text{m}$ was sufficient. On the other hand, a more difficult task was to obtain well-defined microvilli. Pillar-like structures are notoriously difficult to fabricate and typically require careful optimization [73]. Early CEC designs included microvilli with a diameter of $0.2 \mu\text{m}$ and no contour lines. However, AM of such designs resulted in collapsed microvilli with a height significantly below the desired $1 \mu\text{m}$ (Fig. 2h, i). Including one contour line in the CEC design led to the fabrication of microvilli with the desired height. However, it also increased the microvilli diameter from $0.2 \mu\text{m}$ to $0.55 \pm 0.06 \mu\text{m}$. Due to the dense packing of the microvilli, this led to yet another challenge, aggregation (Fig. 2j). Ultimately, in order to fabricate well defined microvilli, the contour count was kept to one line, and the spacing between the microvilli was increased, leading to the AM of the CEC scaffolds shown in the last panel of Fig. 1.

3.3. Preparation and characterization of polymer-cushioned model cell membranes supported on the manufactured cell scaffolds

The biomimetic polymer-cushioned model cell membrane was prepared using a layer-by-layer protocol based on electrostatic interactions recently developed by Wan et al. [55] A schematic representation of the surface modification steps on a SMC scaffold is shown in Fig. 3. The cell scaffolds were fabricated by 2PP AM using the acrylic-based IP-L 780

photoresist and therefore have a slightly negative surface charge. According to the producer's specifications, the polymerization of the acrylic monomers in the IP-L 780 photoresist proceeds through esterification of the carboxylic acid groups, and only few residual carboxylic acid groups are expected to remain on the surface. On the other hand, PLL is a positively charged polymer widely employed for surface coating and layer-by-layer modification due to its tendency to adsorb onto polar and hydrophilic substrates [74]. In the first surface modification step, PLL is added to structures prepared by 2PP AM of the acrylic-based IP-L 780 photoresist and forms a surface coating layer. In the second surface modification step, dye-loaded DOPC SUV are added to the PLL-coated structures. The SUV spontaneously fuse on the positive surface to form a supported lipid bilayer cushioned by the PLL.

The PLL layer plays a dual role in the biomimetic cell membrane. Firstly, it enables facile surface functionalization based on electrostatic interactions. Secondly, owing to its role as polymer cushion in the system, PLL creates a physical separation between the surface and the lipid bilayer. This should reduce the influence of potential surface defects on the lipid bilayer, and allow the incorporation of transmembrane proteins. The present work did not aim to explore protein incorporation into the polymer-cushioned lipid bilayer, but this type of model cell membrane is known to be particularly suitable for such studies [42].

The CLSM technique was employed to verify the functionalization of the fabricated polymeric cell scaffolds with the fluorescent SUV. The fluorescence of three types of samples was characterized: i) a fully modified sample, where first PLL was added, followed by SUV addition, ii) a sample where SUV were added directly on the fabricated surface,

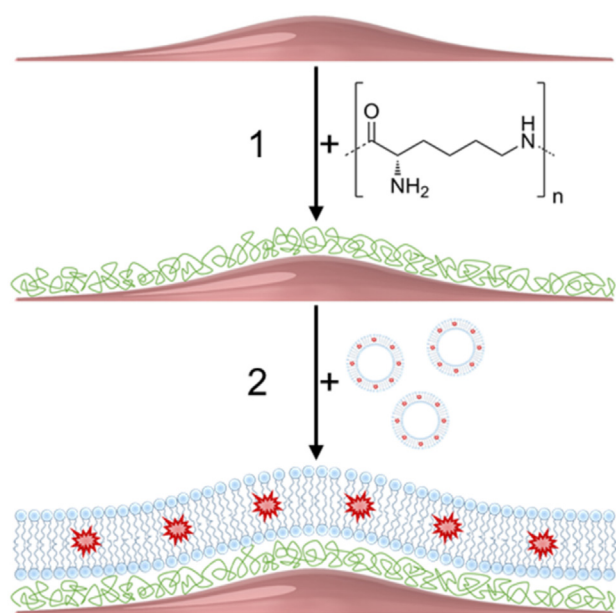


Fig. 3. Schematic representation (not drawn to scale) of the surface functionalization steps involved in preparing the polymer-cushioned model cell membrane on a fabricated structure corresponding to the smooth muscle cell model. In the first step, poly-L-lysine (PLL) adsorbs on the surface of the clean polymeric micropattern. In the second step, dye-loaded small unilamellar vesicles (SUV) fuse on the PLL-modified surface, resulting in a polymer-cushioned lipid bilayer biomimetic membrane.

without PLL, and iii) the unmodified polymer. Fig. 4 shows representative microscopy images of the functionalized scaffolds, including the fluorescence intensity profiles for a small and representative number of structures.

The CLSM images demonstrate successful functionalization with lipids. It can be noted here that the thickness of a DOPC lipid bilayer is of only ~ 4 nm [76], whereas a PLL monolayer coating has a thickness < 1 nm [77]. Given the fact that the fluorescence signal follows the scaffold shape rather well, it can be asserted that the surface functionalization process results in a rather uniform coating with lipids. However, the CLSM images cannot clarify if this is due to the formation of a lipid bilayer or of a multilayer. This aspect was previously elucidated by Wan et al. [55], who concluded that following this surface modification protocol leads to a surface that is covered by a single and continuous lipid bilayer, rather than a multilayer. Importantly, as it can be seen in Fig. 4d, h and l, the reference samples where the PLL coating step was omitted and the SUV were added directly to the polyacrylate surface show significantly less fluorescence. In these reference samples, the weak fluorescence signal can be attributed to the autofluorescence of IP-L 780 rather than the DiI dye. Polymerized IP-L 780 is known to display autofluorescence in the wavelength range 450–550 nm [75]. The DiI dye was selected for this study because it has a fluorescence emission maximum at 565 nm, outside the IP-L 780 autofluorescence wavelength range. A weak autofluorescence signal was nevertheless recorded from the IP-L 780 structures even at 565 nm, and there is no significant difference between this signal and that of the reference samples shown in Fig. 4d, h and l (additional details in Section S5 of the SI). Overall, this confirms the role of PLL in the surface modification process, and that the model cell membrane obtained is a polymer-cushioned lipid bilayer. The mean gray values for the functionalized scaffolds and both corresponding references are shown in Fig. S8 of the SI:

The fluorescence intensity profile follows the shape of the scaffolds (shown in Fig. 1). For the RBC model, the highest fluorescence intensity is measured at the edges of the structures, while the center appears dimmer. For the SMC model, the fluorescence intensity profile shows lower values at the edges of the structures and higher values in the center. In the case of the CEC model, the intensity profile shows a number of

noise-like peaks over the cell body attributed to the presence of the microvilli-like structures. However, the resolution of the $20\times/0.50$ objective is not sufficient to resolve individual microvilli, which lead to the rather rough appearance of the fluorescence intensity profile. Although theoretically a resolution of ~ 200 nm can be achieved using a $100\times/1.40$ oil immersion objective, focusing issues were encountered in practice when using an objective with a magnification higher than $20\times$, which is why the $20\times/0.50$ objective was used instead.

3.4. Flexibility of the fabrication technique

Given the DLW nature of 2PP AM as a fabrication technique, the scaffold parameters can easily be adjusted based on each user's requirements, as long as the technical characteristics of the fabrication equipment are taken into account. For example, Fig. 5 shows scaffolds fabricated using different design parameters than the structures shown in Fig. 1. In Fig. 5a, the SMC units are packed more tightly, ensuring higher surface coverage. While the SMC packing shown in Fig. 1h was preferred for both CLSM and optical profilometry measurements, complete surface coverage might be interesting for some applications. Fig. 5b shows a larger SMC array (1×1 mm²). Large scaffolds, up to several millimeters in lateral size, can be fabricated by stitching smaller print areas, as described in Section S6 of the SI. However, this naturally implies a considerable increase in the AM time, which is ~ 2 h 46 min for the 1×1 mm² array, compared to < 2 min required for printing the 120×120 μm^2 array. Finally, Fig. 5c shows a CEC scaffold where the 20 μm columnar cell body is included in the printing, in addition to the apical side containing the microvilli. Again, this leads to an increase in the printing time, from the ~ 8 s needed to print the apical side of a single model cell, to ~ 136 s needed to print a single CEC including the 20 μm tall columnar cell body.

The structure shown in Fig. 5c was fabricated using a slightly different DLW process compared to all other structures described in this paper. To produce this structure based on the 3D design shown in Fig. 6a, a change in DLW configuration from *oil immersion* to *DiLL* was required to get a good quality print. Printing in *oil immersion* configuration on the Nanoscribe is schematically shown in Fig. 6b. In this case, the laser is focused into the IP-L 780 photoresist placed on the top of a borosilicate glass coverslip through the glass substrate and a layer of Immersol 518F matching the refractive index of the glass. Printing starts on the top surface of the glass coverslip and proceeds upwards. The height of the print is limited to < 190 μm by the focal length of the objective. Furthermore, aberrations increase with height, particularly when the laser is focused through a thick layer of crosslinked photoresist. This can be clearly seen for the 20 μm tall CEC scaffold shown in Fig. 6c, which is significantly deformed, particularly in the top half. An alternative approach, printing in *DiLL* configuration, is schematically shown in Fig. 6d. In contrast with the *oil immersion* process, the photoresist IP-Dip is instead placed on the bottom of a 0.70 mm thick fused silica substrate, and is used as both immersion medium and polymer precursor. Printing starts on the bottom surface of the fused silica substrate and proceeds downwards. In *DiLL* configuration, structures with a height > 300 μm can be fabricated. As the focused laser beam exiting the objective only travels through uncrosslinked resist in this case, aberrations are not influenced by structure height, and the 20 μm tall CEC scaffold shown in Fig. 6e matches the shape of the 3D design very well. Therefore, the *DiLL* configuration and the IP-Dip resist were preferred for fabricating the 20 μm tall CEC structures.

The IP-Dip photoresist is more viscous than IP-L 780 and proper development of the small features is more challenging. Whereas for IP-L 780 development of the uncrosslinked photoresist was done by 20 min incubation in isopropanol, development of the IP-Dip structures was a two-step process comprising 20 min incubation in PGMEA followed by 5 min in isopropanol. Nevertheless, as it can be seen in Fig. 6e, residual polymer fibers can still be noticed for the IP-Dip microvilli structures. Further optimization of the development process for the

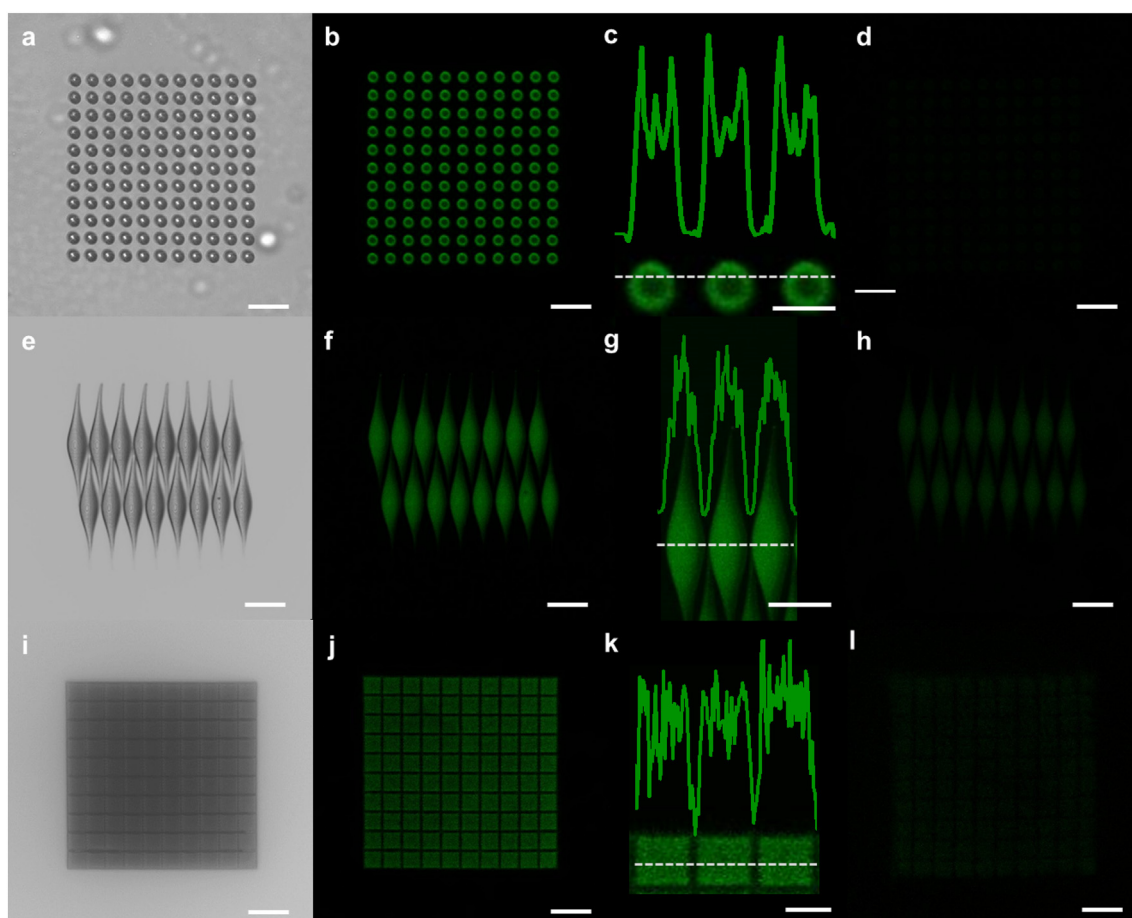


Fig. 4. Images showing the surface-functionalized scaffolds. (a-d) Red blood cell (RBC) model. (e-h) Smooth muscle cell (SMC) model. (i-l) Columnar epithelial cell (CEC) model. (a, e, i) Brightfield images and (b, f, j) confocal laser scanning microscopy (CLSM) images of arrays functionalized with PLL and small unilamellar vesicles (SUV). (c, g, k) Enlarged area showing three cells functionalized with PLL and SUV and the corresponding fluorescence intensity profiles, shown in green. (d, h, l) CLSM images of reference arrays functionalized with SUV (without PLL). The scale bars are 25 μm for all full array samples and 10 μm for all enlarged areas.

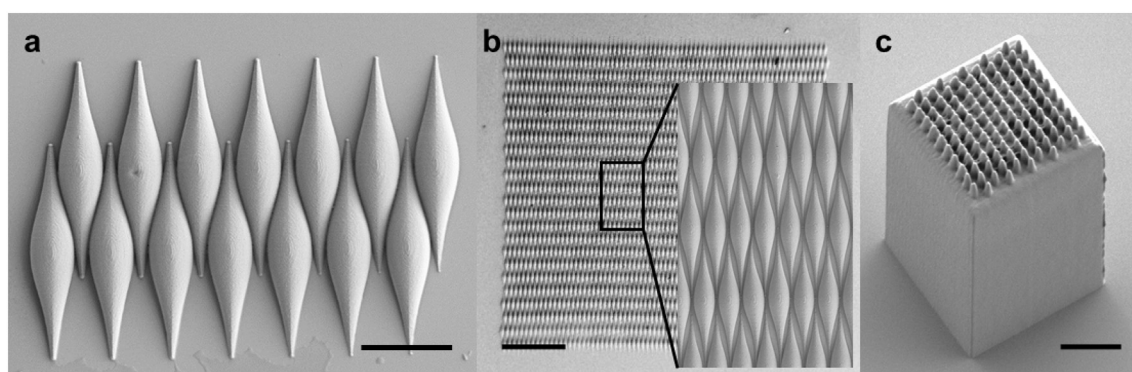


Fig. 5. Scanning electron micrographs of fabricated cell-mimicking scaffolds with varying parameters. (a) Smooth muscle cell scaffold with tight packing, ensuring a high surface coverage, scale bar 25 μm . (b) Smooth muscle cell scaffold with a surface area of $1 \times 1 \text{ mm}^2$, scale bar 200 μm . Inset shows a higher magnification micrograph of the area in the black box. (c) Columnar epithelial cell scaffold including a 20 μm tall columnar cell body below the apical side containing the microvilli, scale bar 5 μm .

IP-Dip microstructures, by e.g. mixing during the incubation or adding an additional incubation step in PGMEA, should help overcome this.

4. Conclusions

This paper demonstrates the feasibility of fabricating model cell membranes that mimic the natural curvature and dimensions of

human cells. Three types of human cells having different shapes, sizes, and distinctive features were chosen, i.e. red blood cells, smooth muscle cells, and columnar epithelial cells with microvilli. The polymeric cell scaffolds were designed and fabricated using two-photon polymerization additive manufacturing. Careful optimization of the design and fabrication steps allowed achieving biomimetic shapes and dimensions. A layer-by-layer surface modification protocol was employed to

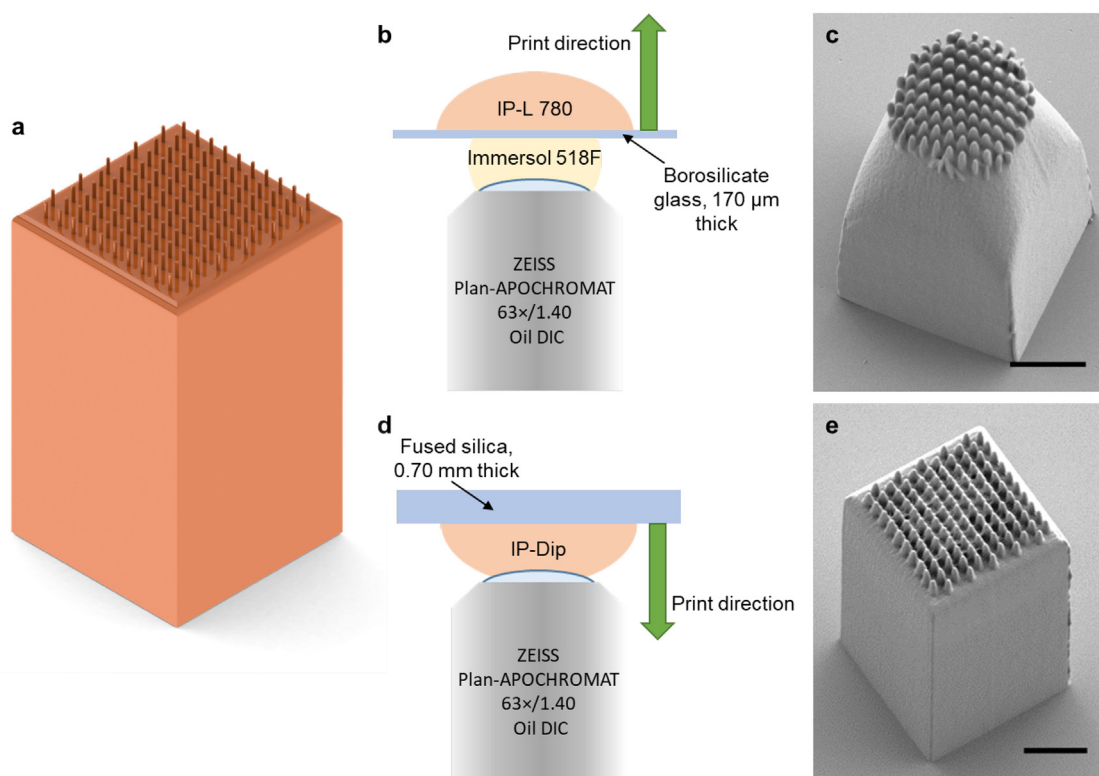


Fig. 6. (a) Columnar epithelial cell (CEC) model including a 20 μm tall body. Comparison between (b, c) oil immersion and (d, e) DiLL printing configurations on the Nanoscribe. (b, d) Schematic representation showing the printing configuration. (c, e) Micrographs of single CEC 20 μm tall structures printed using the two configurations, scale bar is 5 μm .

functionalize the fabricated cell scaffolds and convert them into polymer-cushioned lipid bilayer model cell membranes. For this purpose, the polymeric cell scaffolds were first coated with the cationic polymer PLL and subsequently with an amphiphilic lipid DOPC bilayer doped with the hydrophobic fluorescent dye DiI. The formation of the polymer-cushioned lipid bilayer model cell membrane was confirmed by analyzing fluorescence data acquired using confocal laser scanning microscopy.

While this work is a proof-of-concept demonstration for the fabrication of polymer-cushioned model cell membranes on scaffolds mimicking human cell shapes prepared by AM, the ingredients for developing truly biomimetic model cell membranes based on this approach are also briefly discussed in this paper. The fabrication technique employed, additive manufacturing based on direct laser writing two-photon polymerization, allows for full 3D design freedom featuring critical dimensions down to ~ 200 nm. Together with the choice of photoresists, printing parameters and post-processing methods available, the 3D design freedom with high resolution is expected to enable the fabrication of biomimetic cell membranes mimicking both the shape and mechanical properties of any types of human cells. Such scaffolds that reproduce human cell shapes with high fidelity are expected to be particularly beneficial for drug delivery studies where membrane curvature is an important factor. Furthermore, polymer-cushioned lipid bilayer model cell membranes, such as those presented in this work, are known to be particularly suitable for incorporating transmembrane proteins, which are often of interest in studies where membrane curvature plays an important role. The model cell membrane complexity may be increased by e.g. incorporating proteins or tailoring the bilayer composition. Thus, by tailoring both the fabrication and surface functionalization processes, truly biomimetic cell membranes can be developed based on the approach pioneered herein.

The sub-micrometer resolution enabled by direct laser writing two-photon polymerization complements well the more established macro-scale additive manufacturing techniques for biomedical applications,

such as fused filament fabrication or stereolithography. Altogether, additive manufacturing techniques have the power to revolutionize biomedical research. Interdisciplinary studies involving experts in e.g. engineering, chemistry, materials science, and biology are more likely to provide additive manufacturing solutions to real biological challenges. The polymer-cushioned model cell membranes supported on 3D cell scaffolds presented herein represent a valuable example demonstrating the ever-growing usefulness of additive manufacturing for biomedical research at all size scales.

Data availability

The datasets generated and/or analysed during the current study are available from the corresponding author on reasonable request.

Declaration of Competing Interest

None.

Acknowledgments

The authors acknowledge financial support from the Novo Nordisk Foundation (grant number NNF16OC0021948) and VILLUM FONDEN (grant numbers 00022918 and 34424). The authors would like to thank technician Karina Juul Vissing for the SUV preparation and Assist. Prof. Feng Wan for useful discussions, Dr. Thomas Pedersen and Berit Herstrøm for optical profilometry measurements, and Prof. Niels Bent Larsen, Assoc. Prof. Rodolphe Marie, Assoc. Prof. Nazila Kamaly, Dr. Jong Hyun Lee, and the DTU Nanolab technicians for their help with equipment access and training.

Appendix A. Supplementary data

Supplementary data to this article can be found online at <https://doi.org/10.1016/j.matdes.2021.109486>.

References

- [1] A. Gebhardt, Understanding Additive Manufacturing, Carl Hanser Verlag GmbH & Co, KG, 2011, <https://doi.org/10.3139/9783446431621>.
- [2] Q. Lei, J. He, D. Li, Electrohydrodynamic 3D printing of layer-specifically oriented, multiscale conductive scaffolds for cardiac tissue engineering, *Nanoscale*. 11 (2019) 15195–15205, <https://doi.org/10.1039/c9nr04989d>.
- [3] J. Koffler, W. Zhu, X. Qu, O. Platoshyn, J.N. Dulin, J. Brock, L. Graham, P. Lu, J. Sakamoto, M. Marsala, S. Chen, M.H. Tuszynski, Biomimetic 3D-printed scaffolds for spinal cord injury repair, *Nat. Med.* 25 (2019) 263–269, <https://doi.org/10.1038/s41591-018-0296-z>.
- [4] A.V. Do, B. Khorsand, S.M. Geary, A.K. Salem, 3D printing of scaffolds for tissue regeneration applications, *Adv. Healthc. Mater.* 4 (2015) 1742–1762, <https://doi.org/10.1002/adhm.201500168>.
- [5] J. An, J.E.M. Teoh, R. Suntornnond, C.K. Chua, Design and 3D printing of scaffolds and tissues, *Engineering* 1 (2015) 261–268, <https://doi.org/10.15302/J-ENG-2015061>.
- [6] J. Creff, R. Courson, T. Mangeat, J. Foncy, S. Souleille, C. Thibault, A. Besson, L. Malaquin, Fabrication of 3D scaffolds reproducing intestinal epithelium topography by high-resolution 3D stereolithography, *Biomaterials*. 221 (2019), <https://doi.org/10.1016/j.biomaterials.2019.119404>.
- [7] G. Arrabito, F. Cavaleri, A. Porchetta, F. Ricci, V. Vetri, M. Leone, B. Pignataro, Printing life-inspired subcellular scale compartments with autonomous molecularly crowded confinement, *Adv. Biosyst.* 3 (2019) 1900023, <https://doi.org/10.1002/adbi.201900023>.
- [8] G. Arrabito, V. Ferrara, A. Bonasera, B. Pignataro, Artificial biosystems by printing biology, *Small*. 16 (2020) 1907691, <https://doi.org/10.1002/sml.201907691>.
- [9] M. Carve, D. Wlodkowic, 3D-printed chips: compatibility of additive manufacturing photopolymeric substrata with biological applications, *Micromachines*. 9 (2018) 91, <https://doi.org/10.3390/mi9020091>.
- [10] M.F. Arif, S. Kumar, K.M. Varadarajan, W.J. Cantwell, Performance of biocompatible PEEK processed by fused deposition additive manufacturing, *Mater. Des.* 146 (2018) 249–259, <https://doi.org/10.1016/j.matdes.2018.03.015>.
- [11] S. Bose, D. Ke, H. Sahasrabudhe, A. Bandyopadhyay, Additive manufacturing of biomaterials, *Prog. Mater. Sci.* 93 (2018) 45–111, <https://doi.org/10.1016/j.pmatsci.2017.08.003>.
- [12] M. Touri, F. Kabirian, M. Saadati, S. Ramakrishna, M. Mozafari, Additive manufacturing of biomaterials – the evolution of rapid prototyping, *Adv. Eng. Mater.* 21 (2019) 1800511, <https://doi.org/10.1002/adem.201800511>.
- [13] A.I. Bunea, M.H. Jakobsen, E. Engay, A.R. Bañas, J. Glückstad, Optimization of 3D-printed microstructures for investigating the properties of the mucus biobarrier, *Micro Nano. Eng.* 2 (2019) 41–47, <https://doi.org/10.1016/j.mne.2018.12.004>.
- [14] L.R. Jaidev, K. Chatterjee, Surface functionalization of 3D printed polymer scaffolds to augment stem cell response, *Mater. Des.* 161 (2019) 44–54, <https://doi.org/10.1016/j.matdes.2018.11.018>.
- [15] Z. Lin, M. Wu, H. He, Q. Liang, C. Hu, Z. Zeng, D. Cheng, G. Wang, D. Chen, H. Pan, C. Ruan, 3D printing of mechanically stable calcium-free alginate-based scaffolds with tunable surface charge to enable cell adhesion and facile biofunctionalization, *Adv. Funct. Mater.* 29 (2019) 1808439, <https://doi.org/10.1002/adfm.201808439>.
- [16] R. Zhang, N.B. Larsen, Stereolithographic hydrogel printing of 3D culture chips with biofunctionalized complex 3D perfusion networks, *Lab Chip* 17 (2017) 4273–4282, <https://doi.org/10.1039/c7lc00926g>.
- [17] P.J. Davim, *Additive and Subtractive Manufacturing: Emergent Technologies*, Walter de Gruyter GmbH, Berlin/Boston, 2019 ISBN 978-3-11-054816-7.
- [18] S. Beg, W.H. Almalki, A. Malik, M. Farhan, M. Aatif, Z. Rahman, N.K. Alruwaili, M. Alrobaian, M. Tarique, M. Rahman, 3D printing for drug delivery and biomedical applications, *Drug Discov. Today* 25 (2020) 1668–1681, <https://doi.org/10.1016/j.drudis.2020.07.007>.
- [19] Q. Ge, Z. Li, Z. Wang, K. Kowsari, W. Zhang, X. He, J. Zhou, N.X. Fang, Projection micro stereolithography based 3D printing and its applications, *Int. J. Extrem. Manuf.* 2 (2020) 22004, <https://doi.org/10.1088/2631-7990/ab8d9a>.
- [20] A.K. Nguyen, R.J. Narayan, Two-photon polymerization for biological applications, *Mater. Today* 20 (2017) 314–322, <https://doi.org/10.1016/j.mat.2017.06.004>.
- [21] T. Weiss, G. Hildebrand, R. Schade, K. Liefelth, Two-photon polymerization for microfabrication of three-dimensional scaffolds for tissue engineering application, *Eng. Life Sci.* 9 (2009) 384–390, <https://doi.org/10.1002/elsc.200900002>.
- [22] J. Song, C. Michas, C.S. Chen, A.E. White, M.W. Grinstaff, From simple to architecturally complex hydrogel scaffolds for cell and tissue engineering applications: opportunities presented by two-photon polymerization, *Adv. Healthc. Mater.* 9 (2020) 1901217, <https://doi.org/10.1002/adhm.201901217>.
- [23] X. Wang, Z. Wei, C.Z. Baysah, M. Zheng, J. Xing, Biomaterial-based microstructures fabricated by two-photon polymerization microfabrication technology, *RSC Adv.* 9 (2019) 34472–34480, <https://doi.org/10.1039/c9ra05645a>.
- [24] F. Larramendy, S. Yoshida, D. Maier, Z. Fekete, S. Takeuchi, O. Paul, 3D arrays of microcages by two-photon lithography for spatial organization of living cells, *Lab Chip* 19 (2019) 875–884, <https://doi.org/10.1039/c8lc01240g>.
- [25] N. Hauptmann, Q. Lian, J. Ludolph, H. Rothe, G. Hildebrand, K. Liefelth, Biomimetic designer scaffolds made of D,L-lactide-caprolactone polymers by 2-photon polymerization, *Tissue Eng. Part B Rev.* 25 (2019) 167–186, <https://doi.org/10.1089/ten.teb.2018.0284>.
- [26] D. Bruen, C. Delaney, J. Chung, K. Ruberu, G.G. Wallace, D. Diamond, L. Florea, 3D printed sugar-sensing hydrogels, *Macromol. Rapid Commun.* 41 (2020) 1900610, <https://doi.org/10.1002/marc.201900610>.
- [27] D. Martella, S. Nacentini, C. Parmeggiani, D.S. Wiersma, Photonic artificial muscles: from micro robots to tissue engineering, *Faraday Discuss.* (2020), <https://doi.org/10.1039/d0fd00032a>.
- [28] A. Tudor, C. Delaney, H. Zhang, A.J. Thompson, V.F. Curto, G.Z. Yang, M.J. Higgins, D. Diamond, L. Florea, Fabrication of soft, stimulus-responsive structures with sub-micron resolution via two-photon polymerization of poly(ionic liquid)s, *Mater. Today* 21 (2018) 807–816, <https://doi.org/10.1016/j.mat.2018.07.017>.
- [29] M. Del Pozo, C. Delaney, C.W.M. Bastiaansen, D. Diamond, A.P.H.J. Schenning, L. Florea, Direct laser writing of four-dimensional structural color microactuators using a photonic photoresist, *ACS Nano* 14 (2020) 9832–9839, <https://doi.org/10.1021/acsnano.0c02481>.
- [30] S. Nacentini, D. Martella, C. Parmeggiani, D.S. Wiersma, 3D printed photoresponsive materials for photonics, *Adv. Opt. Mater.* 7 (2019) 1900156, <https://doi.org/10.1002/adom.201900156>.
- [31] M. Colautti, P. Lombardi, M. Trapuzzano, F.S. Piccioli, S. Pazzagli, B. Tiribilli, S. Nacentini, F.S. Cataliotti, D.S. Wiersma, C. Toninelli, A 3D polymeric platform for photonic quantum technologies, *Adv. Quant. Technol.* 3 (2020) 2000004, <https://doi.org/10.1002/qute.202000004>.
- [32] F. Mayer, S. Richter, J. Westhauser, E. Blasco, C. Barner-Kowollik, M. Wegener, Multimaterial 3D laser microprinting using an integrated microfluidic system, *Sci. Adv.* 5 (2019) <https://doi.org/10.1126/sciadv.aau9160> eau9160.
- [33] A. Selimis, V. Mironov, M. Farsari, Direct laser writing: principles and materials for scaffold 3D printing, *Microelectron. Eng.* 132 (2015) 83–89, <https://doi.org/10.1016/j.mee.2014.10.001>.
- [34] A.R. Studart, Additive manufacturing of biologically-inspired materials, *Chem. Soc. Rev.* 45 (2016) 359–376, <https://doi.org/10.1039/c5cs00836k>.
- [35] Y. Yang, X. Song, X. Li, Z. Chen, C. Zhou, Q. Zhou, Y. Chen, Recent progress in biomimetic additive manufacturing technology: From materials to functional structures, *Adv. Mater.* 30 (2018) <https://doi.org/10.1002/adma.201706539>.
- [36] A. du Plessis, C. Broeckhoven, I. Yadroitsava, I. Yadroitsev, C.H. Hands, R. Kunju, D. Bhat, Beautiful and functional: a review of biomimetic design in additive manufacturing, *Addit. Manuf.* 27 (2019) 408–427, <https://doi.org/10.1016/j.addma.2019.03.033>.
- [37] M.I. Abid, L. Wang, Q.-D. Chen, X.-W. Wang, S. Juodkazis, H.-B. Sun, Angle-multiplexed optical printing of biomimetic hierarchical 3D textures, *Laser Photonics Rev.* 11 (2017) 1600187, <https://doi.org/10.1002/lpor.201600187>.
- [38] M. Carlotti, V. Mattoli, Functional materials for two-photon polymerization in microfabrication, *Small*. 15 (2019) 1902687, <https://doi.org/10.1002/sml.201902687>.
- [39] D. Serien, S. Takeuchi, Multi-component microcylinder with 3D spatially defined proteinaceous environment, *ACS Biomater. Sci. Eng.* 3 (2017) 487–494, <https://doi.org/10.1021/acsbomaterials.6b00695>.
- [40] C. Foged, H.M. Nielsen, Cell-penetrating peptides for drug delivery across membrane barriers, *Expert Opin. Drug Deliv.* 5 (2008) 105–117, <https://doi.org/10.1517/17425247.5.1.105>.
- [41] Y. Shan, E.T. Kim, M.P. Eastwood, R.O. Dror, M.A. Seeliger, D.E. Shaw, How does a drug molecule find its target binding site? *J. Am. Chem. Soc.* 133 (2011) 9181–9183, <https://doi.org/10.1021/ja202727y>.
- [42] A.-I. Bunea, S. Harloff-Helleberg, R. Taboryski, H.M. Nielsen, Membrane interactions in drug delivery: model cell membranes and orthogonal techniques, *Adv. Colloid Interf. Sci.* 281 (2020) 102177, <https://doi.org/10.1016/j.cis.2020.102177>.
- [43] Y.-H.M. Chan, S.G. Boxer, Model membrane systems and their applications, *Curr. Opin. Chem. Biol.* 11 (2007) 581–587, <https://doi.org/10.1016/j.cbpa.2007.09.020>.
- [44] T.G. Pomorski, T. Nylander, M. Cárdenas, Model cell membranes: discerning lipid and protein contributions in shaping the cell, *Adv. Colloid Interf. Sci.* 205 (2014) 207–220, <https://doi.org/10.1016/j.cis.2013.10.028>.
- [45] N. Papo, Y. Shai, Can we predict biological activity of antimicrobial peptides from their interactions with model phospholipid membranes? *Peptides*. 24 (2003) 1693–1703, <https://doi.org/10.1016/J.PEPTIDES.2003.09.013>.
- [46] O.G. Mouritsen, Lipids, curvature, and nano-medicine, *Eur. J. Lipid Sci. Technol.* 113 (2011) 1174–1187, <https://doi.org/10.1002/ejlt.201100050>.
- [47] L. Iversen, S. Mathiasen, J.B. Larsen, D. Stamou, Membrane curvature bends the laws of physics and chemistry, *Nat. Chem. Biol.* 11 (2015) 822–825, <https://doi.org/10.1038/nchembio.1941>.
- [48] S. Aimon, A. Callan-Jones, A. Berthaud, M. Pinot, G.E.S. Toombes, P. Bassereau, Membrane shape modulates transmembrane protein distribution, *Dev. Cell* 28 (2014) 212–218, <https://doi.org/10.1016/j.devcel.2013.12.012>.
- [49] J.B. Larsen, K.R. Rosholm, C. Kennard, S.L. Pedersen, H.K. Munch, V. Tkach, J.J. Sakon, T. Bjørnholm, K.R. Weninger, P.M. Bendix, K.J. Jensen, N.S. Hatzakis, M.J. Uline, D. Stamou, How membrane geometry regulates protein sorting independently of mean curvature, *ACS Cent. Sci.* (2020), <https://doi.org/10.1021/acscentsci.0c00419> acscentsci.0c00419.
- [50] L. Leggio, G. Arrabito, V. Ferrara, S. Vivarelli, G. Paternò, B. Marchetti, B. Pignataro, N. Iraci, Mastering the tools: natural versus artificial vesicles in nanomedicine, *Adv. Healthc. Mater.* 9 (2020) 2000731, <https://doi.org/10.1002/adhm.202000731>.
- [51] L. Zhang, L. Hong, Y. Yu, S.C. Bae, S. Granick, Nanoparticle-assisted surface immobilization of phospholipid liposomes, *J. Am. Chem. Soc.* 128 (2006) 9026–9027, <https://doi.org/10.1021/ja062620r>.
- [52] A.D. Bangham, M.M. Standish, J.C. Watkins, Diffusion of univalent ions across the lamellae of swollen phospholipids, *J. Mol. Biol.* 13 (1965) 238–252, [https://doi.org/10.1016/S0022-2836\(65\)80093-6](https://doi.org/10.1016/S0022-2836(65)80093-6).
- [53] B. Mui, L. Chow, M.J. Hope, Extrusion technique to generate liposomes of defined size, *Methods Enzymol.* 367 (2003) 3–14, [https://doi.org/10.1016/S0076-6879\(03\)67001-1](https://doi.org/10.1016/S0076-6879(03)67001-1).
- [54] N.A. Feidenhans'l, P.E. Hansen, L. Pilny, M.H. Madsen, G. Bissacco, J.C. Petersen, R. Taboryski, Comparison of optical methods for surface roughness characterization, *Meas. Sci. Technol.* 26 (2015), 085208, <https://doi.org/10.1088/0957-0233/26/8/085208>.

- [55] F. Wan, T. Nylander, S.N. Klodzinska, C. Foged, M. Yang, S.G. Baldursdóttir, H.M. Nielsen, Lipid shell-enveloped polymeric nanoparticles with high integrity of lipid shells improve mucus penetration and interaction with cystic fibrosis-related bacterial biofilms, *ACS Appl. Mater. Interfaces* 10 (2018) 10678–10687, <https://doi.org/10.1021/acsami.7b19762>.
- [56] T.J. Collins, ImageJ for microscopy, *Biotechniques* 43 (2007) S25–S30, <https://doi.org/10.2144/000112517>.
- [57] M.L. Turgeon, *Clinical Hematology: Theory and Procedures*, 4th Ed Lippincott Williams & Wilkins, 2005.
- [58] J. Feher, *Quantitative Human Physiology | ScienceDirect*, 2nd Ed Academic Press, 2017.
- [59] J.W. Brown, C.J. McKnight, Molecular model of the microvillar cytoskeleton and organization of the brush border, *PLoS One* 5 (2010), e9406, <https://doi.org/10.1371/journal.pone.0009406>.
- [60] S. Saha, V. Nguyen, J. Oakdale, D. Wang, Y. Chang, S. Chen, Scalable submicrometer additive manufacturing, *Science* (80) 366 (2019) <https://doi.org/10.1126/science.aax8760>.
- [61] J.S. Oakdale, J. Ye, W.L. Smith, J. Biener, Post-print UV curing method for improving the mechanical properties of prototypes derived from two-photon lithography, *Opt. Express* 24 (2016) 27077, <https://doi.org/10.1364/oe.24.027077>.
- [62] L.J. Jiang, Y.S. Zhou, W. Xiong, Y. Gao, X. Huang, L. Jiang, T. Baldacchini, J.-F. Silvain, Y.F. Lu, Two-photon polymerization: investigation of chemical and mechanical properties of resins using Raman microspectroscopy, *Opt. Lett.* 39 (2014) 3034, <https://doi.org/10.1364/ol.39.003034>.
- [63] M. Gernhardt, E. Blasco, M. Hippler, J. Blinco, M. Bastmeyer, M. Wegener, H. Frisch, C. Barner-Kowollik, Tailoring the mechanical properties of 3D microstructures using visible light post-manufacturing, *Adv. Mater.* 31 (2019) 1901269, <https://doi.org/10.1002/adma.201901269>.
- [64] J. Bauer, A. Guell Izard, Y. Zhang, T. Baldacchini, L. Valdevit, Thermal post-curing as an efficient strategy to eliminate process parameter sensitivity in the mechanical properties of two-photon polymerized materials, *Opt. Express* 28 (2020) 20362, <https://doi.org/10.1364/OE.395986>.
- [65] M.M. Zieger, Designing Functional 2D and 3D Structures: From Ultrathin Coatings to Laser Lithography, <https://d-nb.info/1182430627/34> 2019.
- [66] A.J. Ford, P. Rajagopalan, Measuring cytoplasmic stiffness of fibroblasts as a function of location and substrate rigidity using atomic force microscopy, *ACS Biomater. Sci. Eng.* 4 (2018) 3974–3982, <https://doi.org/10.1021/acsbomaterials.8b01019>.
- [67] J. Torgersen, X.H. Qin, Z. Li, A. Ovsianikov, R. Liska, J. Stampfl, Hydrogels for two-photon polymerization: a toolbox for mimicking the extracellular matrix, *Adv. Funct. Mater.* 23 (2013) 4542–4554, <https://doi.org/10.1002/adfm.201203880>.
- [68] A. Nishiguchi, H. Zhang, S. Schweizerhof, M.F. Schulte, A. Mourran, M. Möller, 4D printing of a light-driven soft actuator with programmed printing density, *ACS Appl. Mater. Interfaces* 12 (2020) 12176–12185, <https://doi.org/10.1021/acsami.0c02781>.
- [69] A.I. Ciuciu, P.J. Cywiński, Two-photon polymerization of hydrogels-versatile solutions to fabricate well-defined 3D structures, *RSC Adv.* 4 (2014) 45504–45516, <https://doi.org/10.1039/c4ra06892k>.
- [70] N. Chidambaram, R. Kirchner, R. Fallica, L. Yu, M. Altana, H. Schiff, Selective surface smoothening of polymer microlenses by depth confined softening, *Adv. Mater. Technol.* 2 (2017) 1700018, <https://doi.org/10.1002/admt.201700018>.
- [71] G. Seniutinas, A. Weber, C. Padeste, I. Sakellari, M. Farsari, C. David, Beyond 100 nm resolution in 3D laser lithography – post processing solutions, *Microelectron. Eng.* 191 (2018) 25–31, <https://doi.org/10.1016/j.mee.2018.01.018>.
- [72] Y. Bougdid, Z. Sekkat, Voxels optimization in 3D laser nanoprinting, *Sci. Rep.* 10 (2020) 10409, <https://doi.org/10.1038/s41598-020-67184-2>.
- [73] C. Delaney, N. Geoghegan, H. Ibrahim, M. O'Loughlin, B.J. Rodriguez, L. Florea, S.M. Kelleher, Direct laser writing to generate molds for polymer nanopillar replication, *ACS Appl. Polym. Mater.* 2 (2020) 3632–3641, <https://doi.org/10.1021/acscpm.0c00626>.
- [74] J.-H. Choi, S.-O. Kim, E. Linardy, E.C. Dreaden, V.P. Zhdanov, P.T. Hammond, N.-J. Cho, Influence of pH and surface chemistry on poly(L-lysine) adsorption onto solid supports investigated by quartz crystal microbalance with dissipation monitoring, *J. Phys. Chem. B* 119 (2015), <https://doi.org/10.1021/acs.jpcc.5b01553>.
- [75] S. Puce, E. Sciurti, F. Rizzi, B. Spagnolo, A. Quattieri, M. De Vittorio, U. Staufer, 3D-microfabrication by two-photon polymerization of an integrated sacrificial stencil mask, *Micro Nano. Eng.* 2 (2019) 70–75, <https://doi.org/10.1016/j.mne.2019.01.004>.
- [76] D. Regan, J. Williams, P. Borri, W. Langbein, Lipid bilayer thickness measured by quantitative DIC reveals phase transitions and effects of substrate hydrophilicity, *Langmuir* 35 (2019) 13805–13814, <https://doi.org/10.1021/acs.langmuir.9b02538>.
- [77] G.R. Heath, M. Li, I.L. Polignano, J.L. Richens, G. Catucci, P. O'Shea, S.J. Sadeghi, G. Gilardi, J.N. Butt, L.J.C. Jeuken, Layer-by-layer assembly of supported lipid bilayer poly-L-lysine multilayers, *Biomacromolecules* 17 (2016) 324–335, <https://doi.org/10.1021/acs.biomac.5b01434>.